

Force Calculation in 3-D Magnetic Equivalent Circuit Networks With a Maxwell Stress Tensor

Marco Amrhein, *Member, IEEE*, and Philip T. Krein, *Fellow, IEEE*

Abstract—Magnetic equivalent circuit (MEC) models are increasingly valuable for analysis and design of electromechanical devices, particularly electrical machines, because of their moderate computational effort and reasonable accuracy. Force and torque calculations in prior MEC implementations are almost exclusively based on the virtual work method (VWM) adapted to the specific device model. But VWM does not easily extend to a general MEC modeling approach. In this paper, the more direct Maxwell stress tensor (MST) method is applied to a general 3-D MEC modeling framework. MST theory and implementation are presented. Its application is discussed with the example of an electromagnet. Results are compared to both measurements and analytical and finite-element models.

Index Terms—3-D magnetic equivalent circuits (MECs), electromagnet, force calculation, Maxwell stress tensor (MST), modeling of electromechanical devices, virtual work method (VWM).

I. INTRODUCTION

IMPROVEMENT of electrical machine performance is imperative in order to meet new application requirements. Progress made in power electronics allows performance enhancement of current electrical machine designs. The most common types, induction machines, take limited advantage of these recent developments [1], in part because computer-aided design (CAD) tools are inadequate for advanced design. Most CAD tools employ analytical models, which have limited accuracy in performance calculations [2]–[4]. Other tools are based on finite-element analysis (FEA), requiring massive computational efforts for the analysis of each design [5]. Thus, new CAD approaches need to be developed that can incorporate advanced machine performance criteria and overcome limitations of current design tools.

Magnetic equivalent circuits (MECs) have recently become a more popular choice for the analysis and design of electrical machines [6]–[12]. A good introduction to MEC is given in [6]. MEC is considered a compromise between analytical

models and FEA [12]. It is more accurate than analytical analysis tools because of the geometrically based magnetic circuit representation of a device, and requires less computational effort than FEA because the model sizes are smaller [8], [9]. Thus, MECs are well-suited for fast and reliable performance calculations [7]–[9].

If MEC is to be employed as a design tool, an accurate force calculation must be implemented. The literature on force computation in MEC is limited. The most common approach is based on an analytical implementation of the virtual work method (VWM), in which force is computed from a spatial derivative of stored energy. Several authors calculate spatial derivatives of position-dependent air gap reluctances, formulating an analytical expression for force and torque in terms of these derivatives, and the scalar magnetic potential solution [6], [9], [10]. Others implement VWM discretely by evaluating the total system energy difference at two positions, then dividing by the spatial difference [13]. Another approach is based on flux linkages and currents from electrical-equivalent circuit formulas [12]. All these approaches are contingent on a coarse distribution of flux tubes (reluctance paths) in the individual MEC machine model.

VWM is not easily extended to a general 3-D modeling framework [14]. In this paper, the more direct Maxwell stress tensor (MST) method is applied to MEC. MST can be considered because the framework in [14] provides a unique path of integration in an arbitrary-sized reluctance element distribution. Calculation and integration of the MST are addressed in detail. Its application is then shown with the example of an electromagnet. Results are compared to measurements, and to analytical and FEA models. The MST method has been successfully applied to torque calculations in induction machines [15], [16].

II. MST METHOD IN A 3-D MEC FRAMEWORK

A. Reluctance Element Definition

A 3-D reluctance element has been defined [14], [16] that uses six reluctance branches to model a device region. These connect scalar magnetic potential nodes at the element center and boundaries, and represent flux tubes. Flux flows in axial direction along each branch axis. A device can be modeled by distributing these reluctance elements throughout its geometry. The reluctance element definition has been reproduced in Fig. 1 for clarity.

The reluctance element distribution yields a nonlinear system of equations due to nonlinear ferromagnetic material properties (material permeabilities depend on the magnetic field intensity). This nonlinear system of equations is solved using a globally convergent Newton–Raphson method, which is based on [17].

Manuscript received May 25, 2008; revised October 9, 2008. First published June 16, 2009; current version published August 21, 2009. The material is based in part upon work supported by the Office of Naval Research under Award N00014-08-1-0397 and in part by Grainger Center for Electric Machinery and Electromechanics (CEME) at the University of Illinois at Urbana-Champaign. This paper was presented in part at the IEEE Electric Ship Technologies Symposium, Arlington, VA, 2007. Paper no. TEC-00194-2008.

M. Amrhein was with Grainger Center for Electric Machinery and Electromechanics, Department of Electrical and Computer Engineering, University of Illinois at Urbana-Champaign, Urbana, IL 61801 USA. He is now with PC Krause and Associates, Inc., West Lafayette, IN 47906 USA (e-mail: amrhein@ieee.org).

P. T. Krein is with Grainger Center for Electric Machinery and Electromechanics, Department of Electrical and Computer Engineering, University of Illinois at Urbana-Champaign, Urbana, IL 61801 USA (e-mail: krein@uiuc.edu).

Digital Object Identifier 10.1109/TEC.2009.2016142

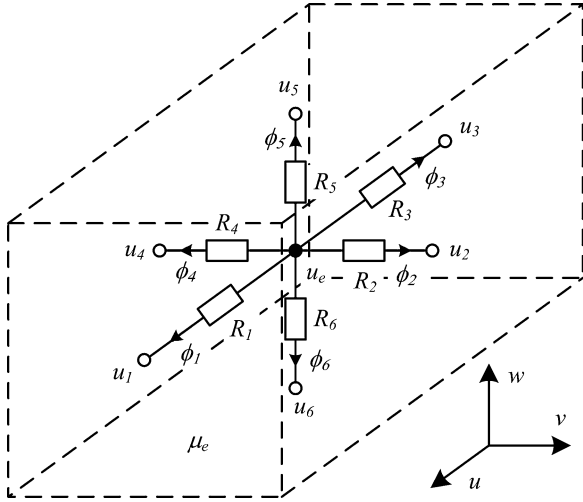


Fig. 1. Passive 3-D reluctance element with six branch reluctances defined in the element flux tube coordinate system $u-v-w$ [14], [16], [18], where u_i , ϕ_i , and R_i are the scalar magnetic potential, flux, and reluctance in branch i , respectively, u_e is the scalar magnetic potential in the element center, and μ_e the element permeability (assumed constant within the element).

Details of the implemented 3-D MEC method are provided in [14]–[16].

B. MST Method

The magnetic field solution on a closed surface around that object is required in order to calculate the exerted force on an object with the MST method. This closed surface defines the integration path S . The force \mathbf{F} is then

$$\mathbf{F} = \oint_S (\mathbf{T}_{MST} \cdot \hat{\mathbf{n}}) dS \quad (1)$$

where $\hat{\mathbf{n}}$ is the normal unit vector on the surface S pointing away from the object and \mathbf{T}_{MST} is the stress tensor

$$\mathbf{T}_{MST}(i, j) = \mu_0 \left(H_i H_j - \frac{1}{2} \delta_{ij} H_i H_j \right). \quad (2)$$

The variables H_i and H_j represent the magnetic field intensities in the global coordinate system of the object, where index variables i and j represent each coordinate system axis. A detailed derivation of the MST method is given in [19].

MST has been used successfully in FEA models [20], but since there is no unique integration path, there is some degree of ambiguity in the force solution [19], [21]. The mesh in FEA does not provide a clearly defined contour, leaving it up to the user to define the integration path. In MEC, the reluctance network surrounding an object provides a unique contour when the element surfaces defined by the flux tubes are considered (see Fig. 2). The magnetic field intensities can be determined from the magnetic scalar potential solution in each flux tube. Denser element meshes yield better magnetic field accuracy, particularly when local saturation is considered. Thus, with a denser mesh, the reliability of force and torque estimations increases [8]. The MEC framework introduced in [14], [16], and [18] allows the creation of the required dense reluctance element distributions, particu-

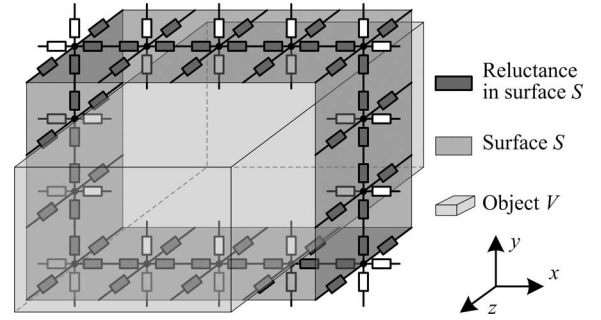


Fig. 2. Integration path (force contour) S defined through the reluctance elements around an object V . The path is uniquely defined by the axis of the reluctance branches in each element.

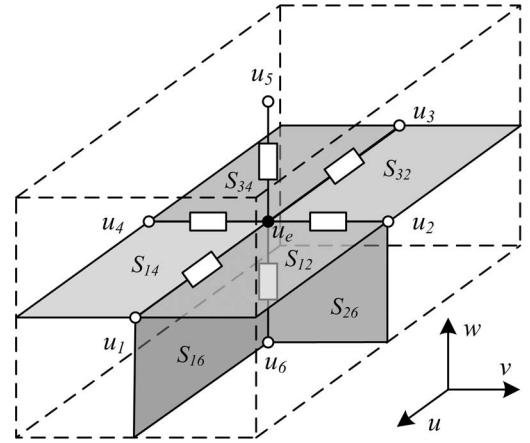


Fig. 3. Integration surface definitions in a reluctance element that is part of the force integration path.

larly in regions of interest such as the air gap of an electrical machine.

C. Implementation of the MST Method

To apply (1) to an MEC model, consider the reluctance network given in Fig. 2. The reluctance elements surrounding the object V form a closed surface S , assuming there are no reluctance elements in front of or behind the object in the z -direction. Within each element, (1) can be written as

$$\mathbf{F}_e = \sum_k \left(\mathbf{T}_{MSTe}^{(k)} \cdot \hat{\mathbf{n}}_e^{(k)} \right) S_e^{(k)} \quad (3)$$

where $\mathbf{T}_{MSTe}^{(k)}$ is the MST on the k th element surface $S_e^{(k)}$. The vector $\hat{\mathbf{n}}_e^{(k)}$ is the normal vector to $S_e^{(k)}$. The total force is then the sum of all elements defining S

$$\mathbf{F} = \sum_e \mathbf{F}_e = \sum_e \left\{ \sum_k \left(\mathbf{T}_{MSTe}^{(k)} \cdot \hat{\mathbf{n}}_e^{(k)} \right) S_e^{(k)} \right\}. \quad (4)$$

$\mathbf{T}_{MSTe}^{(k)}$ must be calculated on the branch reluctance surfaces $S_e^{(k)}$ of all elements that are part of the integration path. Each element has 12 possible integration surfaces, defined by the local coordinate system $u-v-w$ through the branch reluctances. Fig. 3 shows six of the possible 12 integration surfaces. Three or four

TABLE I
MAGNETIC FIELD INTENSITY VECTORS FOR EACH FORCE SURFACE IN A
RELUCTANCE ELEMENT

Element surface	Field intensity vector $\mathbf{H}_{uvw}^{(1)}$	Field intensity vector $\mathbf{H}_{uvw}^{(2)}$
Integration surface in u - v axis		
$S_e^{(12)}$	$[H_1 \ H_2 \ H_3]^T$	$[H_1 \ H_2 \ -H_6]^T$
$S_e^{(14)}$	$[H_1 \ -H_4 \ H_5]^T$	$[H_1 \ -H_4 \ -H_6]^T$
$S_e^{(32)}$	$[-H_3 \ H_2 \ H_5]^T$	$[-H_3 \ H_2 \ -H_6]^T$
$S_e^{(34)}$	$[-H_3 \ -H_4 \ H_5]^T$	$[-H_3 \ -H_4 \ -H_6]^T$
Integration surface in u - w axis		
$S_e^{(15)}$	$[H_1 \ H_2 \ H_3]^T$	$[H_1 \ -H_4 \ H_5]^T$
$S_e^{(16)}$	$[H_1 \ H_2 \ -H_6]^T$	$[H_1 \ -H_4 \ -H_6]^T$
$S_e^{(35)}$	$[-H_3 \ H_2 \ H_5]^T$	$[-H_3 \ -H_4 \ H_5]^T$
$S_e^{(36)}$	$[-H_3 \ H_2 \ -H_6]^T$	$[-H_3 \ -H_4 \ -H_6]^T$
Integration surface in v - w axis		
$S_e^{(25)}$	$[H_1 \ H_2 \ H_3]^T$	$[-H_3 \ H_2 \ H_5]^T$
$S_e^{(26)}$	$[H_1 \ H_2 \ -H_6]^T$	$[-H_3 \ H_2 \ -H_6]^T$
$S_e^{(45)}$	$[H_1 \ -H_4 \ H_5]^T$	$[-H_3 \ -H_4 \ H_5]^T$
$S_e^{(46)}$	$[H_1 \ -H_4 \ -H_6]^T$	$[-H_3 \ -H_4 \ -H_6]^T$

surfaces are part of the integration contour, for example, surfaces S_{12} , S_{14} , S_{32} , and S_{34} , when the integration path follows the u - v plane. (Surface indexes are defined by corresponding boundary node numbers.) When the integration path lies in the u - w plane, surfaces S_{15} , S_{16} , S_{35} , and S_{36} can be defined accordingly (see S_{16} in Fig. 3 as an example). Similarly, in the v - w plane, surfaces S_{25} , S_{26} , S_{45} , and S_{46} can be defined (see S_{26} in Fig. 3 as an example).

The MST (2) is based on magnetic field intensities defined in an orthogonal global coordinate system. Thus, for each surface in the element, the field intensities need to be transformed into the global coordinate system. The six branch field intensities H_b are defined as

$$H_b = \frac{u_e - u_b}{l_b}, \quad b = 1, 2, 3, \dots, 6 \quad (5)$$

where l_b is the distance between scalar magnetic potential nodes u_e and u_b . For the transformation, surface S_{14} is used here as an example. In S_{14} , the participating field intensities are H_1 in the u -axis, H_4 in the v -axis, and H_5 and H_6 in the w -axis. Thus, two sets of global field intensities can be defined, because both w -axis field intensities are part of S_{14} . The local field intensity vectors $\mathbf{H}_{uvw}^{(1)}$ and $\mathbf{H}_{uvw}^{(2)}$ are defined based on to the branch axes orientations

$$\begin{aligned} \mathbf{H}_{uvw}^{(1)} &= [H_1 \ -H_4 \ H_5]^T \\ \mathbf{H}_{uvw}^{(2)} &= [H_1 \ -H_4 \ -H_6]^T. \end{aligned} \quad (6)$$

For the other surfaces $S_e^{(k)}$, these definitions are listed in Table I.

From (6), the global field intensities can be calculated as

$$\begin{aligned} \mathbf{H}_{xyz}^{(1)} &= \mathbf{M}_{CSe} \mathbf{H}_{uvw}^{(1)} \\ \mathbf{H}_{xyz}^{(2)} &= \mathbf{M}_{CSe} \mathbf{H}_{uvw}^{(2)}. \end{aligned} \quad (7)$$

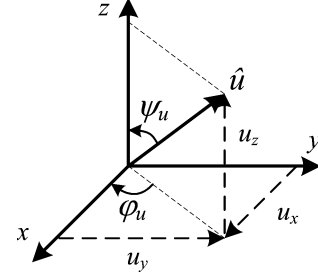


Fig. 4. Angle definitions of unit vector \hat{u} in an orthogonal coordinate system.

In (7), the transformation matrix \mathbf{M}_{CSe} is defined as

$$\begin{aligned} \mathbf{M}_{CSe} &= \begin{bmatrix} \sin(\psi_u) \cos(\varphi_u) & \sin(\psi_v) \cos(\varphi_v) & \sin(\psi_w) \cos(\varphi_w) \\ \sin(\psi_u) \sin(\varphi_u) & \sin(\psi_v) \sin(\varphi_v) & \sin(\psi_w) \sin(\varphi_w) \\ \cos(\psi_u) & \cos(\psi_v) & \cos(\psi_w) \end{bmatrix} \end{aligned} \quad (8)$$

according to the angle definitions given in Fig. 4 between a local coordinate axis (u - v - w) and the global coordinate system (x - y - z). The stress tensor for surface $S_e^{(k)}$ can then be approximated as the average of two stress tensors (2)

$$\mathbf{T}_{MSTe}^{(k)}(i, j) = \frac{1}{2} \mu_0 \left(\begin{aligned} &\mathbf{H}_i^{(1)} \mathbf{H}_j^{(1)} - \frac{1}{2} \delta_{ij} \mathbf{H}_i^{(1)} \mathbf{H}_j^{(1)} \\ &+ \mathbf{H}_i^{(2)} \mathbf{H}_j^{(2)} - \frac{1}{2} \delta_{ij} \mathbf{H}_i^{(2)} \mathbf{H}_j^{(2)} \end{aligned} \right). \quad (9)$$

Thus, the force is calculated by applying (4)–(9).

If the object V in Fig. 2 is rotating around an axis, torque is the product of the tangential force on surface S and the moment arm to the center of rotation. In vector notation, the torque is calculated as the cross product of the distance vector $\hat{\mathbf{r}}$ and the force vector \mathbf{F} . Given the element force vector (3), the torque due to each element can be calculated as

$$\mathbf{T}_e = \hat{\mathbf{r}}_e \times \mathbf{F}_e = \hat{\mathbf{r}}_e \times \sum_k \left(\mathbf{T}_{MSTe}^{(k)} \cdot \hat{\mathbf{n}}_e^{(k)} \right) S_e^{(k)} \quad (10)$$

with $\hat{\mathbf{r}}_e$ being the distance vector between the element center node and the center of rotation. The total torque \mathbf{T} in the global coordinate system is the summation over all elements defining S

$$\mathbf{T} = \sum_e \mathbf{T}_e = \sum_e \left(\hat{\mathbf{r}}_e \times \sum_k \left(\mathbf{T}_{MSTe}^{(k)} \cdot \hat{\mathbf{n}}_e^{(k)} \right) S_e^{(k)} \right). \quad (11)$$

If the global coordinate system does not coincide with the axis of rotation, the torque vector \mathbf{T} needs to be transformed with a transformation matrix similar to (8) to provide a result.

III. EXAMPLE: ELECTROMAGNET

A device has been built and simulated to validate the MST force calculation approach. The device consists of a U-core with an electric coil and an I-core separated by an air gap, as shown in Fig. 5. A magnetic field is established with dc current in the coil, producing an attractive force that pulls the I-core toward the

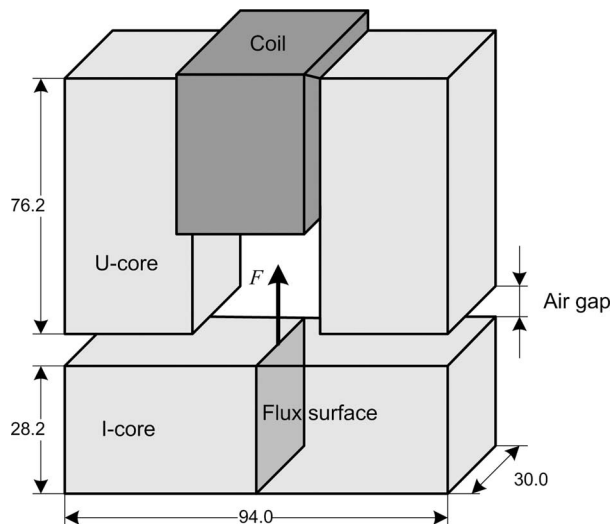


Fig. 5. 3-D electromagnet with U-core and I-core consisting of soft ferrite material 3C90 [22]. The electric coil has 56 turns. Dimensions are in millimeters.

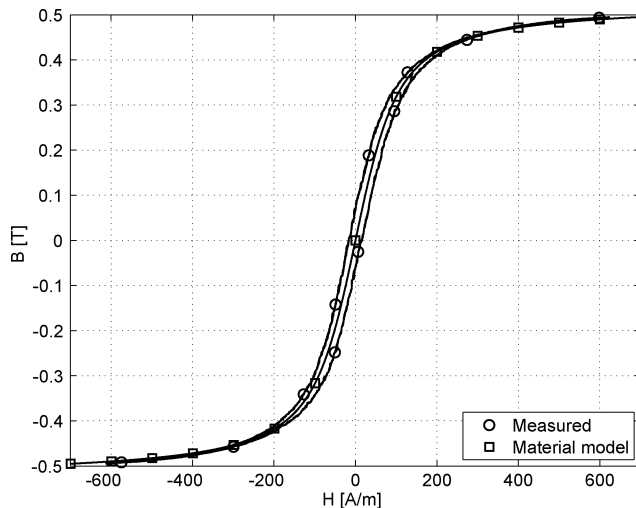


Fig. 6. Measured and modeled magnetization characteristics of soft ferrite material 3C90 [22]. The measurements have been obtained at 60 Hz and room temperature [14].

U-core. Soft ferrite material (Ferroxcube 3C90 [22]) was used, and its measured hysteretic magnetic characteristics and its dc approximation utilized in this paper are shown in Fig. 6. The coil employs 56 turns of 16 AWG magnet wire. It is assumed that the air gap has a fixed value. The force on the I-core is measured for various air gaps and coil currents, and compared to 2-D and 3-D MEC and FEA models, and to two analytical models.

The actual measurement setup is shown in Fig. 7. The U-core is mounted to a fixed structure such that its opening faces down, while the I-core is clamped on a platform attached to a load cell. The attractive force will attempt to lift the I-core, registering a weight decrease in the load cell. The difference between the weight when the coil is turned ON and OFF is the electromechanical force.

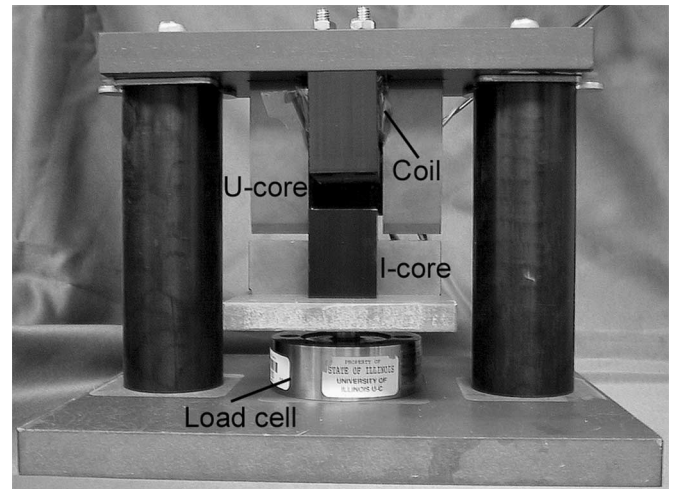


Fig. 7. Experimental setup to measure the force on the I-core.

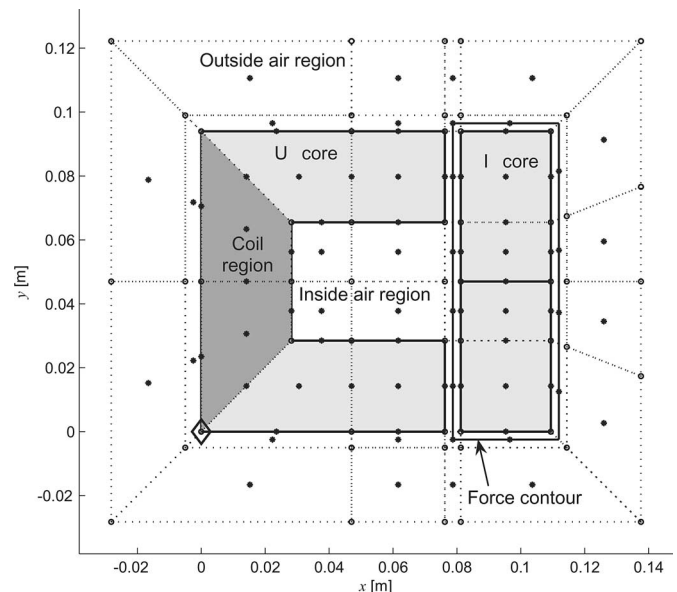


Fig. 8. Initial 2-D reluctance element distribution of the electromagnet with 46 elements. The dotted lines represent the reluctance element outlines.

A. 2-D and 3-D MEC Models

Based on the MEC modeling framework introduced in [14], [16], and [18], 2-D and 3-D MEC models with adjustable reluctance distributions are implemented. The initial 2-D reluctance element distribution (mesh) is shown in Fig. 8. It contains 46 elements. The element boundaries are represented by dotted lines, and the potential nodes are black dots. Only the first few element layers in the air region close to electromagnet are shown. The air region around the magnetic material is extended 500 mm beyond the U-core to capture leakage flux outside the cores. Six mesh parameters define the element distribution and are freely adjustable, yielding great flexibility in creating different meshes with various element sizes. The force contour for the MST method is defined around the I-core, as indicated in Fig. 8.

The 3-D MEC model is a straightforward extension of the 2-D model. The 2-D model can be treated as one slice in the

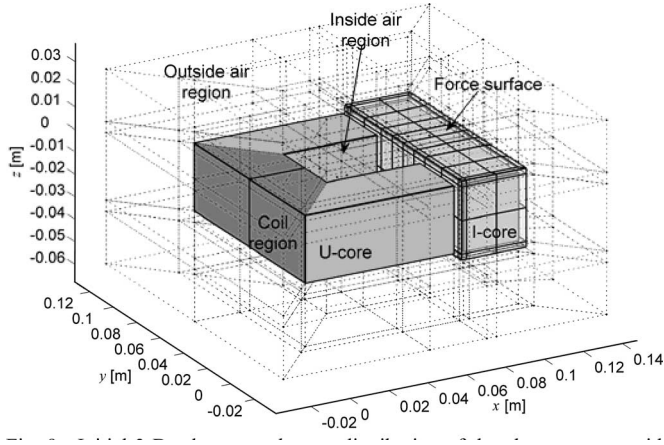


Fig. 9. Initial 3-D reluctance element distribution of the electromagnet with 230 elements, including the force contour around the I-core. The dotted lines represent the reluctance element outlines.

z -plane of the 3-D model. The 3-D reluctance elements are created by stacking multiple slices and connecting parallel element surfaces. Additional mesh parameters describe the number of slices in the cores. As in the 2-D model, the air region outside the electromagnet is extended 500 mm. The initial mesh, which employs 230 elements, is shown in Fig. 9. The force contour, based on surface segments, is defined around the I-core.

B. Force Comparison

Measured and simulated forces for three different air gaps and various MMF values are compared in Fig. 10. The measured force values include measurement error bounds that have been derived from tolerance information given in datasheets of the load cell and the associated strain gage measurement unit. The analytical models calculate the force based on the spatial coenergy derivative. One of them employs a leakage flux correction term, which has been chosen such that the force values match the measurements. The other analytical model neglects leakage completely, and can be viewed as the upper bound of the force solution.

The refined 2-D and 3-D MEC models in the comparison employ 4664 elements and 31 488 elements, respectively. The meshes have a larger number of elements than the initial meshes given in Figs. 7 and 8 to increase the accuracy of the solution (similar to mesh refinement in FEA). The element distributions employed in these MEC models are of structural nature. Mesh refinement is achieved by dividing existing elements in multiple new elements. This approach is simple, but yields large meshes with many new elements that do not add to force-solution accuracy. In the future, it is planned to incorporate more sophisticated mesh algorithms similar to the ones used in FEA, specifically unstructured 2-D quadrilateral and 3-D hexahedral meshes. The emphasis here is on a proof of concept of force calculation with MST.

The 2-D and 3-D FEA models have been implemented in Ansoft's Maxwell software, and employ 6300 and 41 000 elements, respectively (the numbers vary slightly for different

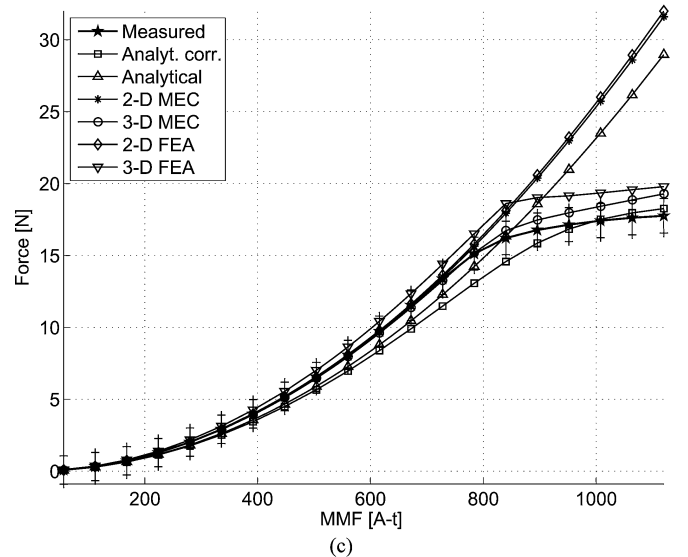
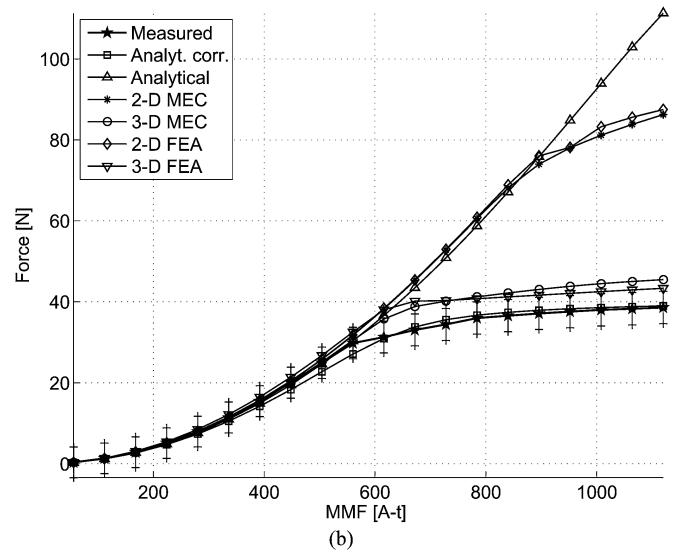
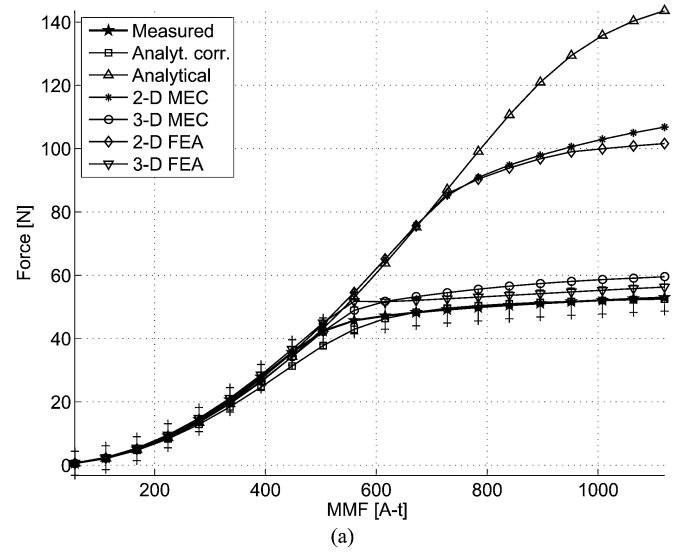


Fig. 10. Comparison of measured and simulated force of the electromagnet for three different air gaps. (a) 1.194 mm. (b) 1.60 mm. (c) 3.302 mm.

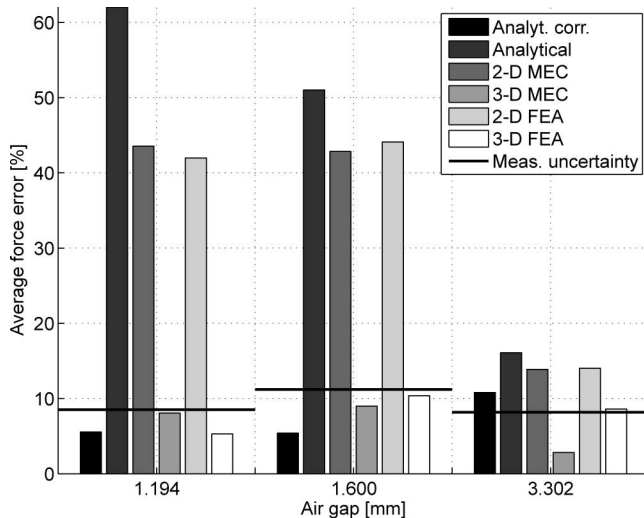


Fig. 11. Average relative force error of simulated force as compared to measured force of the electromagnet for three different air gaps. The measurement uncertainty is calculated as the average maximum relative error of each force measurement.

air gap values). All models use the same soft ferrite material parameters, derived from measured material characteristics.

The results in Fig. 10 indicate that all the models work well when no saturation occurs. This is not surprising, as most of the flux is concentrated in the cores, and leakage effects should be small. Once saturation occurs, only the corrected analytical, and the 3-D MEC and FEA models provide an accurate solution. The 2-D models overestimate the force in the saturated condition. This can be explained by the additional leakage paths considered in the third dimension of the 3-D models. Fig. 11 shows the average relative force error of each model for each air gap. The 2-D FEA and 2-D MEC models have similar average errors of 42% for the 1.194 and 1.600 mm air gaps, and 15% for the 3.302 mm air gap. The error for the 3.302 mm air gap is smaller because saturation occurs at a larger MMF value compared to the smaller air gaps. Because a significant force error is not introduced until saturation occurs, the error is smaller across the whole MMF range. The 3-D FEA and MEC models have errors up to 10%, but are within the uncertainty of the force measurement.

Taking a closer look at the 3-D FEA results in Fig. 10, one can see that the 3-D FEA force rate increase changes abruptly as initial saturation occurs (see Fig. 12 for the 3-D FEA and 3-D MEC results). This is in contrast to the gradual change in the force increase rate observed in the measurements and both MEC models. A similar effect can be seen in the 2-D FEA model when saturation occurs at air gaps of 1.194 and 1.600 mm: the rate changes abruptly at excitations of 700 Ampere-turns (A-t) and 900 A-t, respectively. Various meshes and solution approaches did not alter this nonphysical behavior, leading to the conclusion that initial material saturation is not well-handled in this FEA software. To explain this in detail, consider the underlying formulation of FEA and MEC. In FEA, the solution is sought through minimization of the system energy [23]. If the minimization error during an iterative process becomes

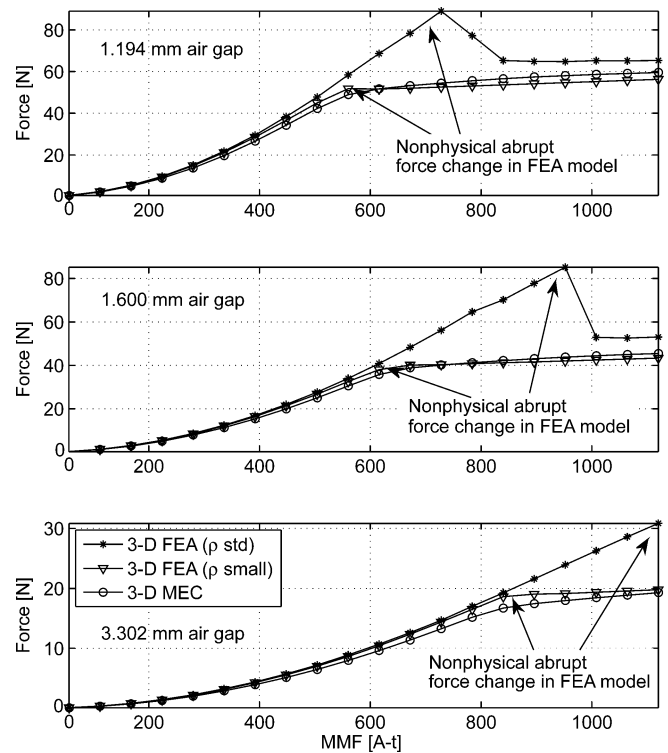


Fig. 12. Nonphysical behavior of simulated 3-D FEA force compared to 3-D MEC force of the electromagnet for three different air gaps.

smaller than a threshold value, it is assumed that the solution converged. However, energy convergence does not automatically imply force accuracy [19]. A lower convergence threshold value improves solution accuracy. Fig. 12 supports this claim, where two sets of 3-D FEA results are shown: one set utilizes the standard convergence threshold of this commercial tool (ρ standard), and the second set utilizes a convergence threshold (ρ small) that is two orders of magnitudes smaller (the results of the latter set are also shown in Fig. 10). However, a threshold value yielding insufficient results would be hard to detect in an iterative design process. MEC does not have this energy convergence issue because it is formulated with circuit relations based on Gauss's law. Convergence occurs not when the minimum energy point is achieved but rather when the flux error in each node is smaller than a certain threshold. This threshold value is directly related to the field solution and force accuracy.

IV. CONCLUSION

The advent of MECs in the analysis and design of electromechanical devices requires the development of a general MEC modeling framework that can be applied to various structures, similar to what has been done with FEA. Part of this development is accurate performance calculation, particularly, forces and torque. Previous efforts are almost exclusively based on VWM in conjunction with specialized models for the individual device to be simulated. However, VWM does not scale well to the general MEC framework introduced in [14], [16], and [18]. Here, the more direct MST method was considered, and its implementation was presented. Accuracy was verified through

comparing force calculations for 2-D and 3-D MEC models of an electromagnet with measurements, and analytical and FEA models. The MEC models require refinement to capture leakage flux accurately, but show appropriate physical behavior as the modeled device was pushed deep into saturation. Based on the results, it is expected that the MST approach should yield reasonably accurate results when applied to electrical machine models.

REFERENCES

- [1] T. A. Lipo, "Novel reluctance machine concepts for variable speed drives," in *Proc. 6th Mediterranean Electrotechnol. Conf.*, 1991, pp. 34–43.
- [2] C. G. Veinott, *Theory and Design of Small Induction Motors*. New York: McGraw-Hill, 1959.
- [3] P. L. Alger, *Induction Machines, Their Behavior and Uses*. New York: Gordon and Breach, 1970.
- [4] T. A. Lipo, *Introduction to AC Machine Design*, vol. 1. Madison, WI: Power Electronics Research Center, University of Wisconsin, 1996.
- [5] T. W. Preston and J. P. Sturgess, "Implementation of the finite-element method into machine design procedures," in *Proc. Int. Conf. Electr. Mach. Drives*, 1993, pp. 312–317.
- [6] V. Ostović, *Dynamics of Saturated Electric Machines*. New York: Springer-Verlag, 1989.
- [7] J. Perho and E. Ritchie, "Analysis of a permanent magnet machine using reluctance network," in *Proc. Int. Conf. Electr. Mach. (ICEM)*, 1996, pp. 44–48.
- [8] C. B. Rasmussen and E. Ritchie, "A magnetic equivalent circuit approach for predicting PM motor performance," in *Proc. Rec. IEEE Ind. Appl. Soc. Ann. Meeting*, 1997, pp. 10–17.
- [9] P. Sewell, K. J. Bradley, J. C. Clare, P. W. Wheeler, A. Ferrah, and R. Magill, "Efficient dynamic models for induction machines," *Int. J. Numer. Model.*, vol. 12, pp. 449–464, 1999.
- [10] H. Meshgin-Kelk, J. Milimonfared, and H. A. Toliyat, "A comprehensive method for the calculation of inductance coefficients of cage induction machines," *IEEE Trans. Energy Convers.*, vol. 18, no. 2, pp. 187–193, Jun. 2003.
- [11] A. C. Koenig, J. M. Williams, and S. D. Pekarek, "Application of evolutionary programming to optimize the rotor pole geometry of a wound rotor synchronous machine," in *Proc. IEEE Power Eng. Soc. General Meeting*, 2004, pp. 1968–1971.
- [12] S. D. Sudhoff, B. T. Kuhn, K. A. Corzine, and B. T. Branecky, "Magnetic equivalent circuit modeling of induction motors," *IEEE Trans. Energy Convers.*, vol. 22, no. 2, pp. 259–270, Jun. 2007.
- [13] J. D. Law, T. J. Busch, and T. A. Lipo, "Magnetic circuit modelling of the field regulated reluctance machine. Part I: Model development," *IEEE Trans. Energy Convers.*, vol. 11, no. 1, pp. 49–55, Mar. 1996.
- [14] M. Amrhein, "Induction machine performance improvements—Design-oriented approaches," Ph.D. dissertation, Dept. Electr. Comput. Eng., Univ. Illinois at Urbana-Champaign, 2007.
- [15] M. Amrhein and P. T. Krein, "Magnetic equivalent circuit simulations of electrical machines for design purposes," in *Proc. IEEE Electr. Ship Technol. Symp.*, 2007, pp. 254–260.
- [16] M. Amrhein and P. T. Krein, "Magnetic equivalent circuit modeling of induction machines—Design-oriented approach with extension to 3-D," in *Proc. IEEE Int. Electr. Mach. Drives Conf.*, 2007, pp. 1557–1563.
- [17] W. H. Press, S. A. Teukolsky, W. T. Vetterling, and B. P. Flannery, *Numerical Recipes in C: The Art of Scientific Computing*, 2nd ed. Cambridge, U.K.: Cambridge Univ. Press, 1992.
- [18] M. Amrhein and P. T. Krein, "Three-dimensional magnetic equivalent circuit framework for modeling electromechanical devices," *IEEE Trans. Energy Convers.*, vol. 24, no. 2, 2009. DOI: 10.1109/TEC.2009.2016134.
- [19] S. J. Salon, *Finite Element Analysis of Electrical Machines*. Norwell, MA: Kluwer, 1995.
- [20] Z. Ren, "Comparison of different force calculation methods in 3D finite element modelling," *IEEE Trans. Magn.*, vol. 30, no. 5, pp. 3471–3474, Sep. 1994.
- [21] A. Benhama, A. C. Williamson, and A. B. J. Reece, "Force and torque computation from 2-D and 3-D finite element field solutions," *Proc. IEE, Electr. Power Appl.*, vol. 146, no. 1, pp. 25–31, Jan. 1999.
- [22] Ferroxcube. (2004). 3C90 material specification [Online]. Available: <http://www.ferroxcube.com/prod/assets/3c90.pdf>
- [23] P. P. Silvester and R. L. Ferrari, *Finite Elements for Electrical Engineers*, 3rd ed. Cambridge, U.K.: Cambridge Univ. Press, 1996.



Marco Amrhein (S'02–M'08) received the Fach-Hochschul-Diploma in electrical engineering from Zurich University of Applied Sciences, Winterthur, Switzerland, in 2000, and the M.S. and Ph.D. degrees in electrical engineering from the University of Illinois at Urbana-Champaign, Urbana, in 2003 and 2007, respectively.

During 2001, he was a Research Engineer at Zurich University of Applied Sciences. In 2007, he joined PC Krause and Associates, Inc., West Lafayette, IN. His current research interests include

all aspects of electrical machines, drives, and power electronics, with emphasis in machine design.

Dr. Amrhein was listed twice in the University of Illinois "Incomplete List of Teachers Ranked as Excellent." He was a Student Leader of the Future Energy Challenge Team, University of Illinois, in 2003, which won second place overall. In 2004, he was awarded the Reid Fellowship, given to an outstanding student with an interest in an academic career. In 2007, he received the Harold L. Olesen Student Award, which is given to an outstanding teaching assistant, and a Grainger Outstanding Power Student Award.



Philip T. Krein (S'76–M'82–SM'93–F'00) received the B.S. degree in electrical engineering and the A.B. degree in economics and business from Lafayette College, Easton, PA, and the M.S. and Ph.D. degrees in electrical engineering from the University of Illinois at Urbana-Champaign, Urbana.

He was an Engineer with Tektronix, Beaverton, OR. He is with the University of Illinois at Urbana-Champaign, where he currently holds the Grainger Endowed Director's Chair in electric machinery and electromechanics as Professor and Director of the Grainger Center for Electric Machinery and Electromechanics.

He has authored an undergraduate textbook *Elements of Power Electronics* (Oxford University Press, 1998). In 2001, he helped to initiate the International Future Energy Challenge, a major student competition involving fuel cell power conversion and energy efficiency. His current research interests include all aspects of power electronics, machines, drives, and electrical energy, with emphasis on nonlinear control approaches. He holds 12 U.S. patents with additional patents pending.

Dr. Krein is a Registered Professional Engineer in Illinois and Oregon. During 1997–1998, he was a Senior Fulbright Scholar at the University of Surrey, U.K., and was recognized as a University Scholar in 1999, the highest research award at the University of Illinois. During 1999–2000, he was the President of the IEEE Power Electronics Society. From 2003 to 2004, he was a member of the IEEE Board of Directors. He is an Associate Editor of the IEEE TRANSACTIONS ON POWER ELECTRONICS. In 2003, he received the IEEE William E. Newell Power Electronics Award.